Performance of an Adaptive Feature-Based Processor for a Wideband Ground Penetrating Radar System

PETER A. TORRIONE

CHANDRA S. THROCKMORTON

LESLIE M. COLLINS, Senior Member, IEEE
Duke University

A two-stage algorithm for landmine detection with a ground penetrating radar (GPR) system is described. First, 3-D data sets are processed using a computationally inexpensive pre-screening algorithm which flags potential locations of interest. These flagged locations are then passed to a feature-based processer which further discriminates target-like anomalies from naturally occurring clutter. Current field trial (over 6500 square meters) and blind test results (over 39000 square meters) are presented and these show at least an order of magnitude improvement over other radar system-based detection algorithms on the same test lanes.

Authors' address: Dept. of Electrical and Computer Engineering, Duke University, Box 90291, Durham, NC 27708, E-mail: (lcollins@ee.duke.edu).

I. INTRODUCTION

Landmines are a constant threat to people across the globe. According to United Nations estimates, there are currently between 60 and 70 million landmines buried in seventy different countries. Every year these landmines claim 26,000 victims, and many of these victims are children [1, 2]. Furthermore, landmine remediation is often plagued by high false alarm rates (FARs) which impede the timely and effective removal of potential threats.

Many subsurface sensing technologies have been proposed for landmine remediation. These include electromagnetic induction sensing (EMI) [3–7], ground penetrating radar (GPR) [8–11], acoustic-to-seismic coupling [12], and neutron backscattering [13]. Until recently the measured responses from GPRs suffered from high radar cross section, and low signal-to-noise ratios (SNRs) making robust detection of small subsurface anomalies difficult. Despite these short comings, a significant body of work applying GPR phenomenology to subsurface landmine detection exists [8–11, 14]. However, FARs in these studies have typically suffered due to the problems inherent to most GPR systems.

Many different approaches have been taken to subsurface landmine detection in GPR data. These include image inversion and synthetic aperture techniques for image enhancement [15–19], principal component analysis (PCA) and independent component analysis (ICA) techniques [10], and hidden Markov models [11]. Several adaptive algorithms have also been applied to the problem including adaptive differences of Gaussians [20], HANOVA techniques [21], 2-D matrix filtering [22], contrast stretch techniques [23], and Kalman filtering [14, 24].

Significant research on feature-based target discrimination has also been performed for both the unexploded ordnance problem [8, 25] as well as for the landmine problem. Feature-based processors using wavelets [26, 27], complex resonances [28], Gaussian mixture models [29], fuzzy sets [30, 31], and order statistics [32] have all been explored previously.

We expand on the existing literature with an adaptive pre-screener built around the least mean squares (LMS) algorithm for subsurface anomaly detection. We also generate features based on visibly observable characteristics of GPR landmine responses for target discrimination using the Wichmann/Niitek GPR. Several different approaches have been considered for processing data from the NIITEK radar including techniques for SNR improvement [33], PCA approaches [34], and feature extraction [35].

The algorithm developed is implementable in a physically realizable system consisting of the Wichmann/Niitek radar mounted on a vehicle with antitank mine overpass abilities. The vehicular system is also equipped with global positioning system

(GPS) sensors to accurately track the system's location. A marking system to be implemented will be mounted on the rear of the vehicular system and will be responsible for marking locations at which our algorithms make target declarations. The work presented here focuses on developing algorithms which process digital data recorded from the Wichmann/Niitek antennae and provide a link between the antennae (mounted in front of the vehicle) and the target marking system. These algorithms provide a translation from large sets of 3-D radar images produced by the antennae to binary yes/no declarations as required by the marking system.

The Wichmann/Niitek radar [36] is a very wideband (200 MHz to 7 GHz) impulse radar with extremely low radar cross section. Thus, the radar implicitly solves many of the aforementioned problems previously associated with subsurface discrimination using GPR based systems. Furthermore, due to the high bandwidth of this radar, accurate phenomenology of buried objects can often be discerned including some of their inner structure. This has lead us to hypothesize that subsurface target identification and discrimination may be possible using the signals measured with this radar system. However target discrimination is often too computationally expensive to meet the real-time requirements of this, a vehicular system.

These real-time requirements have led us to develop a two-stage algorithm which is divided into pre-screening and feature-processing stages. The goal of the pre-screening stage is to quickly flag potential locations of interest and to pass these locations along to the feature-processor. The feature-processor will then attempt to separate targets from naturally occurring clutter and make final decisions regarding the confidence values for each of the alarms presented by the pre-screener. Thus the amount of data which is analyzed by the feature processor is limited by the number of alarms the pre-screener generates. Ideally, the splitting of data processing into two stages should allow for more complicated feature-based discrimination algorithms to operate on the small subset of pre-screener-flagged data in a real-time manner. We present results from field and blind tests generated by both the pre-screener and the pre-screener followed by the feature-based processor.

The remainder of this paper is organized as follows. In Section II we present a brief overview of the Wichmann/Niitek GPR system and the data collection procedures used. In Section III we present an overview of the algorithm structure used in this work and detail the creation of an adaptive pre-screening algorithm built around the LMS algorithm for anomaly detection. In Section IV we discuss the feature-based algorithm we have developed. In Section V we present results from both

TABLE I
Wichmann/Niitek Radar Operating Modes

Mode	Frequency Band	Characteristics
1	200 MHz–7 GHz	Must be near ground and not too wet or deep; best for discrimination
2	200 MHz–5 GHz	2 to 16 inches from ground
3	200 MHz–1 GHz	2 to 16 inches from ground

Note: All data used in this work was collected in mode 1.

Fig. 1. Wichmann/Niitek vehicle-mounted GPR at a western U.S. test site.

field and blind tests, and Section VI contains our conclusions.

II. SENSOR SYSTEM, DATA COLLECTION, AND SCORING

In this section we discuss the Wichmann/Niitek radar system, data collection techniques, and the scoring process used for all training and blind lanes.

A. Sensor System

The Wichmann/Niitek GPR system [36] consists of a vehicle-mounted wide-bandwidth impulse radar integrated with a marking and GPS system. The radar is 1.2 m wide and contains 24 channels spaced approximately 5 cm apart. The radar is capable of operating in three different modes, summarized in Table I. All the data used in this work was collected in mode 1 at a sensor to ground height of 10 in.

As can be seen in Fig. 1, the actual GPR is mounted some distance in front of a wheeled vehicle. As the vehicle moves in the down-track direction all 24 of the radar's channels are sampled once every 5 cm and at each down-track position each channel measures one 417-element time-domain vector.

Sample unprocessed data from an eastern U.S. site is shown in Fig. 2. This image shows 600 down-track GPR responses from a central antenna channel. Clearly the largest source of GPR response energy
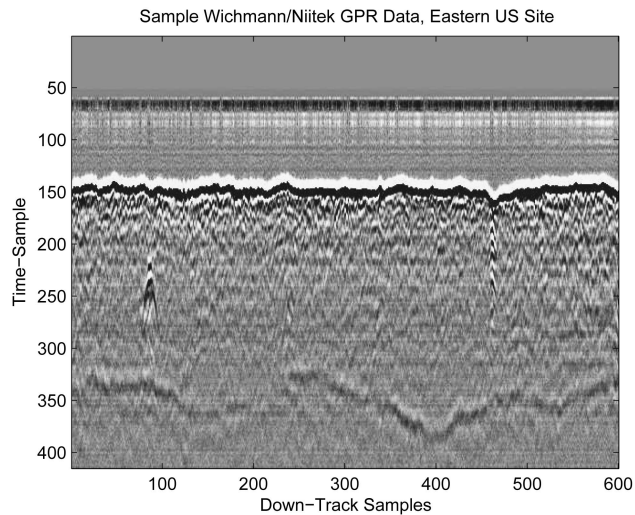
Fig. 2. Sample GPR responses from eastern U.S. site. The x-axis represents down-track scan number, y-axis represents time sample. Two anomalies are visible in this data slice—one at approximately sample 90, and another near sample 460. Also note the high energy of ground bounce visible in all down-track scans near time sample 150. This data has been clipped to enhance contrast.

Fig. 3. Data collection technique to handle difference between Wichmann/Niitek radar cross-track width (1.2 m) and testing lane width (3 m).

is the dielectric discontinuity between the air and ground, seen near time sample 150 in all down-track scans. Despite the ground response, one can still visually identify two subsurface anomalies at scans 90 and 460.

More information regarding the Niitek radar can be obtained at the Niitek website [36].

B. Data Collection

For training and testing purposes, antitank landmines are buried on government-sponsored test sites across the U.S. Results presented in this work are from data collected at two such sites: one temperate eastern U.S. site, and one arid western U.S. site.

Generally targets are buried at these sites in long, prepared strips known as lanes. These lanes were designed for vehicular system testing which assumes that the system will scan an entire 3 m wide road at once. Although one goal for the Wichmann/Niitek radar is integration into a 3 m wide system, the current Wichmann/Niitek prototype radar used in this work is only 1.2 m wide. Thus, in order to collect data encompassing all of any particular 3 m wide lane, data is collected in 3 overlapping 1.2 m strips as illustrated in Fig. 3. These three strips of data for any particular lane are always collected in the same direction.

C. Scoring

The Wichmann/Niitek radar is equipped with a global positioning satellite (GPS) system which constantly monitors the radar's absolute location. This location data is stored along with the radar responses
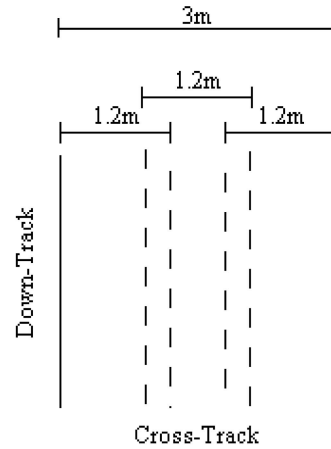
and can be used for accurate alarm placement and scoring. For training and testing purposes, locations of the discrete alarms from different detection algorithms are recorded using the GPS coordinates of the nearest channel/down-track scan location. Since the ground truth for calibration and blind lanes are also known in terms of GPS coordinates, recording alarm locations in the same coordinate system simplifies algorithm scoring.

Since GPS positioning is not exact, and due to the nature of target responses in GPR data, alarms generally need not be placed directly over a target for the target to be considered detected. Usually as long as an alarm falls within a small region around a potential target (often referred to as a "halo") the alarm is considered a hit, and the target is considered to be detected. For this particular radar, an independent contractor determined the smallest viable halo radius to be 0.25 m. In other words, alarms which fall within a quarter meter of the edge of a target are considered "hits." All scores presented in this work were generated with the suggested 0.25 m halo.

Recall that since the width of the Wichmann/Niitek radar does not match the width of the testing lanes, data must be collected in three separate but overlapping strips. Collecting data in this manner may increase FARs since natural false alarm inducing clutter may be encountered twice in two separate 1.2 m wide strips resulting in "multiple looks" on the same subsurface anomaly. Furthermore, since GPRs can "see" outside the physical cross-track footprint of the radar, responses from a single target can often be detected in more than one pass near a target even when the target is not located within the physical footprint of the radar. Since it is difficult for an alarm placement algorithm to reliably and accurately place alarms for objects outside of the radar's footprint, alarms resulting from multiple looks at a single
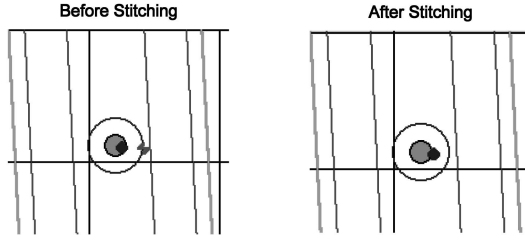
Fig. 4. One hit and one false alarm before stitching resulting in single hit after stitching. Target is represented by filled grey circle. Ring around target is target halo. Hits are represented by small black circles, and false alarm is a small sideways "z" in leftmost image. Diagonal lines represent lane borders and other (irrelevant) markers. Images taken from CTMS [37].

target may lie slightly outside the target's detection halo.

To help remedy the multiple look problem, alarm stitching is performed after data processing and before scoring. Stitching is accomplished by combining two or more alarms which are within a "stitching radius" of one another into one alarm. The resulting alarm has decision statistic equal to the maximum of the individual decision statistics, and it's location is a weighted average of the original alarm locations. The process of stitching continues until no alarms are within a stitching radius of one another. Stitching can fuse two false alarms into a single false alarm, or combine a false alarm which is just outside a target halo with a hit which is within the target halo as shown in Fig. 4. In general, although stitching does provide slight performance gains, it does not radically improve performance. A comparison of stitching results is provided in the results section. Unless otherwise noted, results shown here have been stitched using a stitching radius of 0.5 m.

III. PRE-SCREENING

As mentioned in the introduction, the goal of utilizing a pre-screening algorithm is to minimize the amount of data which a more complicated discrimination algorithm will be required to process. By only applying the discrimination algorithm to a small subset of available data, more complicated algorithms can be run in a real-time manner. A flow chart describing the basic program operation is shown in Fig. 5. The pre-screener operates on all the NIITEK data measured, and the feature-based processor only processes those areas which may contain an anomaly.

In this work we adapted a 2-D adaptive LMS algorithm for anomaly detection with the NIITEK GPR system. The 2-D LMS algorithm has been studied rather extensively [38–40], however to maintain low FARs in NIITEK data, several pre- and post-processing steps must be incorporated. This section is divided into three subsections each detailing either pre-processing, application of the LMS algorithm, or post-processing aspects of the
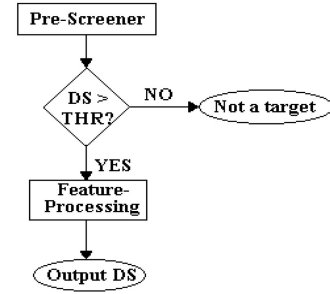

Fig. 5. Overall program flow chart. All GPR data is presented to pre-screening algorithm which then outputs a decision statistic (DS). If the DS is below a specified threshold, the location is declared "target free," otherwise data is passed to feature-based processor which further processes the local area around pre-screener alarm, and outputs a final DS.

TABLE II
Prescreener Tunable Parameters with Current Default Values for Wichmann/Niitek Radar Operating in Mode 1

Ground bounce remove	10 depth samples
Time clipping remove	30 depth samples
Depth segment length	10 depth samples
Median filter size	3 down-track by 3 depth samples
μ	1
LMS guard-band	1 down-track sample
LMS data selection mask	3 down-track samples by 7 cross-track samples
Depth segment whitening guard-band	2 down-track samples
Depth segment whitening data selection	5 down-track samples by 24 cross-track samples
Hamming window length	20 depth segments
2-D whitening guard-band	0 down-track samples
2-D whitening guard-band	8 down-track samples by 24 cross-track samples

pre-screening algorithm. Whenever appropriate, parameters that may be highly dependent on a particular radar collection or strategy have been made "tunable" and their default settings for the NIITEK radar operating in mode 1 are listed in Table II. The entire algorithm flow chart can be seen in Fig. 6.

A. Pre-Processing

Any operations performed on the NIITEK data prior to application of the LMS algorithm are considered pre-processing. The goals of pre-processing are effective ground-bounce removal, suppression of extraneous noise, and separation of data into statistically similar depth bins.

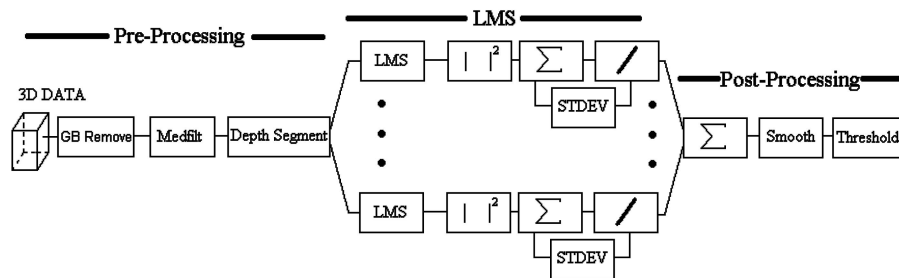1) *Data Aligning*: The large dielecteric discontinuity between soil and air is commonly

Fig. 6. This figure shows overall flow of LMS-anomaly detection algorithm discussed in this paper. Algorithm execution flows from left to right, starting with 3-D data set and ending with a series of alarm locations and confidence values. Pre-processing consists of aligning (not shown), ground-bounce removal, median filtering, and depth segmenting. After depth segmenting, LMS processing and whitening can be performed in parallel on each depth segment, and post-processing follows.

referred to as "ground bounce" and is a major source of interference in GPR signals [41]. As can be seen in Fig. 2 the time sample at which the ground bounce is first recorded is not the same for all down-track or cross-track positions. Several factors can affect the time sample at which the ground bounce is first recorded. Obviously, small variations in the distance from the soil to the radar resulting from actual surface phenomenology will manifest themselves as changes in the time sample at which the ground bounce is recorded. Furthermore, for vehicular systems where the radar is mounted some distance in front of the wheel base, small changes in the soil at the location of the vehicle's wheels will cause significant shifts in the antennae location relative to the ground. These shifts are not symptomatic of the true soil phenomenology, but are an artifact of the vehicle mounted nature of the system.

To correct for the ground bounce shifts incurred by vehicular systems, a simple method of aligning each individual vector to a mean ground bounce peak location is utilized. The current peak location is determined using the maximum value of the time-domain response. While this technique may slightly warp subsurface phenomenology, the resulting certainty with respect to ground-bounce location allows pre-screeners to detect subsurface anomalies with significantly lower FARs than are otherwise attainable.

2) *Ground-Bounce Removal and Time-Clipping*: As the primary undesirable energy source in GPR signals, removal of ground bounce has been the subject of study [41, 42]. However, most of the algorithms proposed rely on somewhat computationally expensive methods for ground bounce removal and are therefore not well suited to a real-time pre-screening algorithm.

Also, since we have already aligned the ground bounce to a mean location (Section IIIA1) it is relatively easy to remove a substantial portion of the ground-bounce response by simply ignoring all data that is a pre-determined number of samples past the mean ground-bounce location. Clearly, ignoring data prior to a certain time sample incurs the risk of

ignoring important information regarding shallow buried targets. However in our experience, NIITEK responses from shallow buried targets reverberate deep into the ground and are generally not in danger of being ignored as long as the number of time samples to ignore is chosen conservatively. The number of samples past the mean ground response is a tunable parameter and is currently set to 10.

Furthermore, as GPR signals propagate through soil, they lose energy and SNRs degrade. Also, as the signals propagate, the NIITEK radar receives responses from depths beyond the locations at which landmines are typically buried. Data at these time samples should be ignored since their SNRs are low and they reflect phenomenology at a depth which is not of interest. In this work we ignore these samples by time-clipping GPR responses at a certain number of samples before the end of each vector. The number of samples at the end of each vector to be ignored is a tunable parameter which is currently set at 30 samples.

3) *Median Filtering (GPS Interference Removal)*: As discussed above, the NIITEK antennae is equipped with a GPS system which is used for algorithm scoring. However, the very wideband nature of the radar leaves it susceptible to types of interference that would not affect other radars. Thus, on occasion the GPS system generates very high energy and very high frequency speckle noise in one to three channels of radar data.

Median filters are a popular method to remove speckle noise while maintaining shape edges, so a median filter is applied to all the data to remove this unwanted speckle noise and simultaneously smooth the data. Since multiple neighboring cross-track channels may be simultaneously corrupted, the median filter is oriented along the depth and down-track directions. Fig. 7 shows one example of the GPS interference before and after median filtering. The size of the median filter applied to the GPR data is a tunable parameter and is currently set to 3 down-track samples by 3 depth samples.

4) *Data Depth-Segmenting*: As the impulse GPR signals propagate through the soil they lose energy.
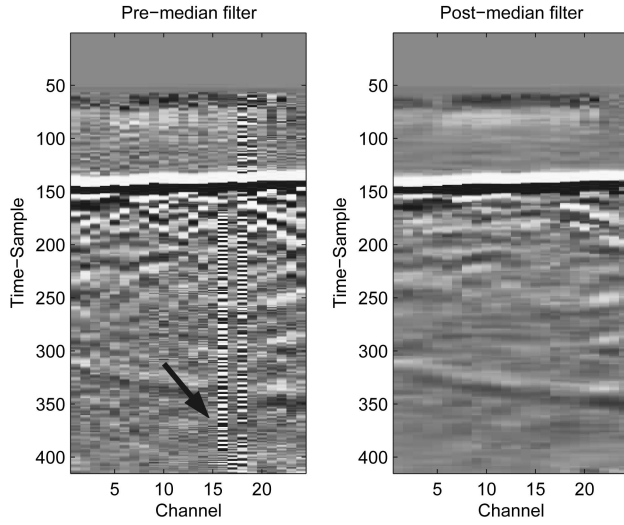
Fig. 7. GPS interference in Wichmann/Niitek GPR data before and after median filtering. Median filtering suppresses GPS interference while maintaining shape edges. In each image, x-axis represents cross-track direction, y-axis represents time axis. Ground bounce clearly visible at time scan 140. Data has been clipped to enhance contrast.
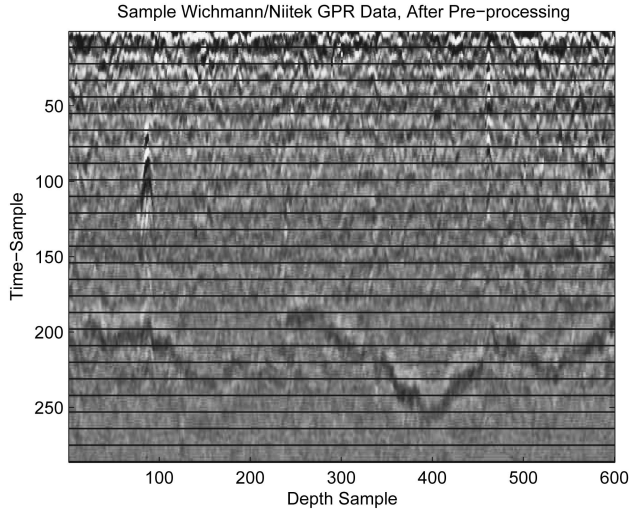

Fig. 8. GPR data after pre-processing. Pre-processing includes ground-bounce aligning, ground-bounce removal, time clipping, median filtering, and depth segmenting. Horizontal black lines represent depth segment demarcations. Image has been clipped to enhance contrast.

Thus responses from deeply buried large anomalies will have less energy when compared with very small but shallow anomalies. This discrepancy will result in high FARs when deeply buried targets need to be identified. It may be possible to use adaptive whitening techniques to mitigate these effects, but forming adaptive estimates of signal variance is computationally expensive and may be hampered by the presence of clutter and potential targets. One way to mitigate the effects of signal propagation is by segmenting data into depth bins over which there is little change in energy.

In this work, the length of the individual depth segments is a tunable parameter and is currently set to 10 time samples. The overall energy of the GPR signals does not change dramatically over this small range of time samples, and each depth segment can be processed independently.

Fig. 8 shows the same data as Fig. 2 after it has been subject to the entire series of pre-processing steps.

B. 2-D LMS

After pre-processing, we apply the 2-D LMS algorithm to each depth bin to generate decision statistics. As previously noted, the 2-D LMS algorithm has been studied rather extensively, although it has not been applied to anomaly detection in GPR data. The LMS algorithm is well known (see for example [43]), and a brief review is presented here. At time n, consider an input vector $\mathbf{u}_n$, a data point of interest d_n, and a tap weight vector $\mathbf{w}_n$. Following these naming conventions, the LMS algorithm operates as

follows:

$$y_n = \mathbf{w}_n^T * \mathbf{u}_n \tag{1}$$

$$e_n = d_n - y_n \tag{2}$$

$$\mathbf{w}_{n+1} = \mathbf{w}_n + \mu * \mathbf{u}_n * e_n. \tag{3}$$

In (1) an adaptive estimate y_n of the point of interest d_n is formed by filtering the input vector $\mathbf{u}_n$ with tap weight vector $\mathbf{w}_n$. In (2) the error e_n between the actual point of interest d_n and the estimate from (1) (y_n) is calculated. Finally, in (3) the updated weight vector $\mathbf{w}_{n+1}$ is calculated by combining the current weight vector $\mathbf{w}_n$ with a correction term calculated using the error e_n, the input vector $\mathbf{u}_n$, and a scaling term μ.

To apply the LMS algorithm to a 3-D set of GPR data, consider a point of interest located in a 3-D depth segment. For each of these points, a 2-D guard-band data selection mask is applied and the data selected by the mask is reshaped into a vector to become the input to the LMS algorithm ($\mathbf{u}_n$). The data selection mask that is used is shown in Fig. 9. The data selection mask and number of guard-band samples surrounding the location of interest are tunable parameters defined in Table II. Since this application is a vehicular system, the data selection mask can be noncausal as long as a decision can be made regarding a particular point before the marking system that trails the vehicle has passed that point. The net noncausality for the full pre-screening algorithm is approximately 1.2 m, which is well within the limitations of this system. Also, the μ parameter in the LMS algorithm is a tunable parameter that is currently set to 1.

At every point, the output of the LMS algorithm is the prediction error at that point or the difference
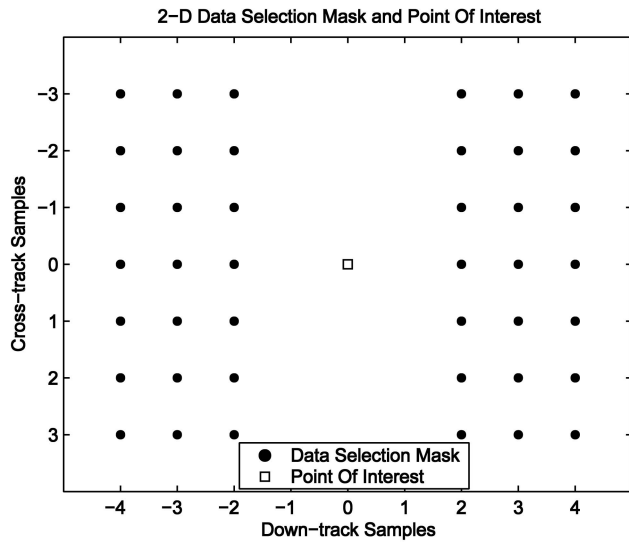
Fig. 9. Data selection mask and point of interest. Selection mask elements shown with circles, point of interest shown with a square. The x-axis represents down-track direction, y-axis represents cross-track direction. Axes numbered relative to location of interest.

between the point of interest and the input vector filtered by the tap weights (e_n from (2)). The prediction error is thus a measure of how poorly the location of interest corresponds to the LMS algorithm's prediction at that point. This process is repeated for each depth sample in a given depth bin, then the net error over the depth bin is calculated by squaring and summing the prediction errors from each depth sample in the bin. These depth bin prediction errors are used to generate the final pre-screener algorithm decision statistic once they have been post-processed.

C. Post-Processing

The goal of the post-processing stages of the LMS pre-screener algorithm is to map the prediction errors from each depth bin into a single confidence value at each down-track/cross-track location. This is accomplished through guard-band whitening, summing, and smoothing.

1) *Depth Segment Whitening*: Although the depth segments have been chosen so that there is little energy variation between samples in a single depth segment, the net energies in different depth segments are likely to be quite different from one another. In order to equalize the depth segment decision statistics prior to fusing, each depth segment is guard-band whitened.

Guard-band whitening is accomplished by forming adaptive estimates of the mean μ_{gb} and standard deviation σ_{gb} of each depth segment decision statistic. These estimates are generated using a data selection mask similar to that described in Section IIIB. Whitening is then accomplished by subtracting the

guard-band mean estimate and dividing the result by the guard-band standard deviation estimate

$$e_{norm} = \frac{e - \mu_{gb}}{\sigma_{gb}}. \qquad (4)$$

The size of the depth-segment guard-band data selection matrix is a tunable parameter and is currently set as shown in Table II.

2) *Depth Segment Convolution and Fusion*: In order to generate a single 2-dimensional decision statistic for a test lane, the individual depth segments need to be combined into a single confidence map. This is accomplished by summing the separate depth segment decision statistics in depth. However, due to landmine phenomenology we know a priori that responses from targets will be spatially correlated in depth, so prior to summation the depth segment decision statistics are convolved with a Hamming window to accentuate anomalies which are correlated in depth. The length of the Hamming window is a tunable parameter and is currently set to 20 depth segments.

3) *2-D Confidence Map Whitening and Smoothing*: Once the depth segment decision statistics have been summed into a single confidence map, it is important to mitigate the effects of different soil types and weather conditions on the resulting decision statistics. Responses from very dry soil types, for example, tend to have lower net energies, and the resulting unprocessed decision statistics represent that. The opposite is true of wet soil.

Ideally we would like to apply a single threshold to our pre-screener decision statistics as in Fig. 5. With this goal in mind, we again apply guard-band whitening to the resulting 2-D confidence map (see Section IIIC1). A local-mean smoothing filter followed by a Gaussian filter is also applied to reduce spurious false alarms and increase the shape-dependent detection of anomalies. The size of the guard-band selection mask is tunable and is shown in Table II.

4) *Discrete Alarm Generation*: Finally, to generate discrete alarms from the 2-D confidence map, the map is thresholded (zeroed where below a given threshold), and alarms are placed at the centers of the remaining 8-connected areas. The decision statistic at each centroid is set to the maximum value of the decision statistics across the relevant area.

IV. FEATURE-BASED PROCESSING

The difficult task for this processor is to preserve the high performance already achieved by LMS as a pre-screener while discarding as many false alarms as possible. Human observers are often quite successful at visually detecting landmines while excluding false alarms, and this processor aims to take advantage of

some of the more simplistic visual features that a human observer might use in addition to the outputs of autonomous anomaly detectors. The features from anomaly detectors used in this processing were the confidence levels from LMS and the output of a CFAR-like (constant FAR) algorithm developed by the University of Florida [44, 45].

Consider the example of a landmine GPR signal displayed in Fig. 10. The GPR signals for each sensor are plotted versus time for a single down-track position after ground bounce removal has been performed. The image demonstrates several features that were incorporated into the feature-based processing. The first feature assesses the amount of reverberation of the object in time as well as the stability of its location, i.e., the reverberation location is centered at a relatively constant cross-track position. For an example of how this feature varies for different objects, consider the simulated example in Fig. 11. The top two plots show hypothetical down-track-slice images—in one, a hyperbolic shape; in the other, a random assortment of high energy concentrations. Visually, the latter would be rejected as being too disjoint to be considered a landmine. Algorithmically, this is achieved by looking at depth (time-sample) slices. On the left, the four depth slices show high energy concentrations ("objects") all of which are centered in approximately the same location (down-track and cross-track). On the right, the four depth slices have the exact same objects; however, they are scattered in down-track and cross-track position. The lack of consistency in object location for depth slices would result in a low confidence that this data indicates a landmine, despite the high energy contained in this data.

Similarly, the second feature assesses the coherence and the size of the object in cross-track position. Although the position of each element of the reverberation varies in time (ideally forming a hyperbolic curve), the curve is generally connected in the cross-track direction. Thus, cross-track slices can be used to track object location. Size was considered important due to the types of targets to be detected, namely antitank landmines; thus, smaller objects would be considered less likely to be landmines.

Finally, an object such as the one shown in Fig. 10 that has a noticeably strong response with respect to the background is considered more likely to be a mine. This last feature's main drawback is that deeply emplaced mines, with low signal amplitudes due to depth, may be less likely to be correctly labeled mines. However, each feature is rated independently, and it is through consideration of all of the features that a confidence value is assigned. The caveat of all of these "observable" features is that their intent is to discard false alarms obvious to the human observer. These features do not address clutter that produce GPR responses and features similar to landmines.
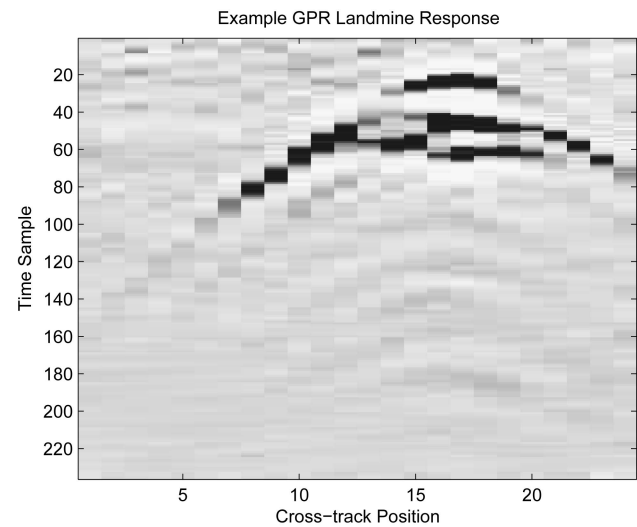

Fig. 10. Typical example of GPR landmine response. The x-axis is cross-track, or channel, number and y-axis is time sample. Image has been clipped to enhance contrast. Observable features utilized by feature-based processor are reverberation of the response, size, and coherence of response in cross-track direction, and relative strength of response with respect to background.

The three features are determined as follows. The depth feature (amount of reverberation) is determined by considering the most prominent object (the object with the greatest area) in time-sample slices. A list is created of the sample slices in which the most prominent object is located in approximately the same position with respect to cross-track and down-track. The length of this list is the depth feature. The cross-track feature (coherence and size of object in cross-track) is determined in a manner similar to the depth feature. Slices are taken in the cross-track dimension, and a list is created of the cross-track slices in which the prominent object remains in relatively the same position. In this case, however, to accommodate the changing shape of the curve, the prominent object is not required to remain in the same position across all slices, but rather, is required to be within a certain distance of the prominent object from the previous slice. Thus, the curve is tracked over its course. The length of the list of tracked objects is the cross-track feature. For both of these features, a greater length is considered to indicate an increased likelihood that the object is a mine.

Lastly, rather than considering the amplitude of the object signal per se, the amplitude feature instead considers the signal strength relative to the background. This was done by considering the number of independent objects with amplitudes within 50% of the peak amplitude. If the alarm has a strong signal strength relative to background, then few, if any other objects will have amplitudes within 50% of the peak amplitude. Consider the simulated example in Fig. 12. The top two plots show two hypothetical situations. On the left is a strong signal response
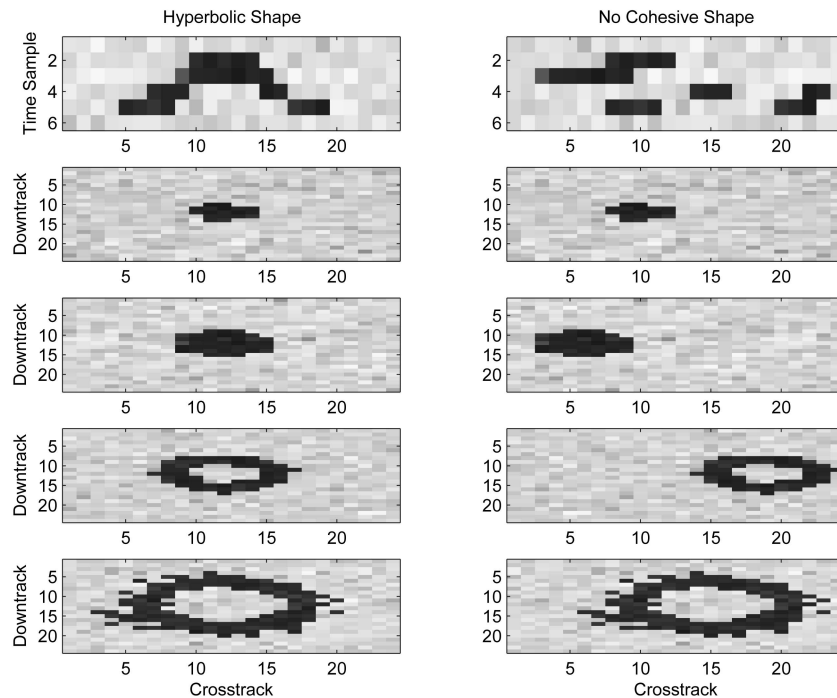
Fig. 11. Demonstration of depth slices and consistency versus lack of consistency in location of depth-slice objects. In first column, a general hyperbolic shape is simulated. In second column, the same depth data are used but shifted randomly so that each layer is no longer aligned. Top two images show down-track slice in data—visually, the right-hand column clearly does not represent a coherent object despite the high energy contained in the data. The next four plots in each column show depth slices. In left-hand column, the objects in the depth slices are clearly aligned, while in right-hand column, their positions are random with respect to each other. The depth feature attempts to exploit this information by tracking the location of objects in depth slices. The lack of alignment in right-hand column would give a low depth-feature score for this alarm.
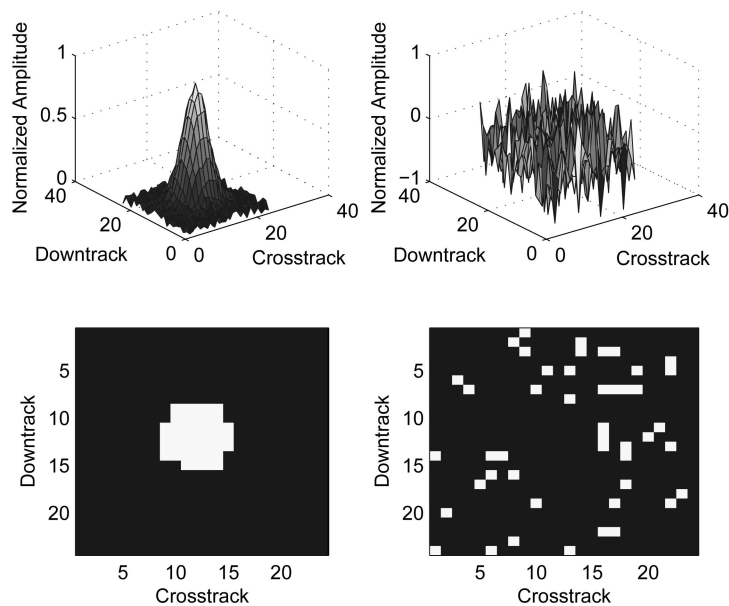

Fig. 12. Demonstration of using the number of objects to determine signal strength relative to background level. The top two plots show a high energy concentration in a noisy background (left) and a selection of noise (right). In the bottom two plots, all amplitudes within 50% of peak amplitude are set to one, while all amplitudes below 50% of peak amplitude are set to zero. For the high energy concentration, only one object occurs, however, for the noise, many small, independent objects occur.

in a noisy background; on the right is background noise alone. The bottom two plots demonstrate the result of setting all amplitudes below 50% of the peak amplitude to zero, and all values above or equal to 50% of the peak amplitude to one. On the left, only one object occurs, while on the right, many independent objects occur. In this study, the number of objects were determined for center cross-track

and down-track slices and combined into one value by

$$A = (D^2 + C^2)^{1/2} \qquad (5)$$

where A is the amplitude feature, D is the number of objects in the central down-track slice, and C is the number of objects in the central cross-track slice. Unlike the other two features, a larger value for this feature is considered to indicate an increased likelihood that the object is a false alarm.

These three features, in addition to the confidence values from LMS and the CFAR-like algorithm, were then each independently mapped, based on calibration data, to scores ranging from 0 to 1. This mapping provides a normalization of the features such that no one feature dominates the determination of the final confidence value. The construction of the scoring function relies on the confidence values of both landmines and false alarms. An extremely low (or zero) FAR from the pre-screener for the calibration data provides too little information for the successful construction of the scoring functions.

Once scores have been determined for each alarm, these scores are weighted and summed to create a final confidence value. The weighting of each feature was based on ranking the features in terms of the likelihood that a particular feature would accurately discriminate between mines and false alarms. Thus, the weighting also depends on adequate training data, as different sites or weather conditions might affect which features provide the best independent performance. The weights were determined using an ordered statistic such that the final confidence value for each alarm ranged from 0 to 1.

V. RESULTS

We have had opportunities to run the aforementioned algorithms on calibration and blind lanes at government managed test sites in both the eastern and western U.S. (under temperate and arid conditions, respectively). Both calibration (known ground truth) and blind (unknown ground truth) test results are presented in this section.

A. Calibration Results

For calibration lanes, algorithms were run as soon as data collected by Niitek became available. Scores were generated using the Counter Mine Test Management System [37]. An overview of the calibration data collections is shown in Table III.

Results for the pre-screener operating alone and the pre-screener operating with feature-based post-processing are presented for both blind and calibration lanes when enough training data for the feature-based processor was available. For reference,

TABLE III
Calibration Data Collection Specifics

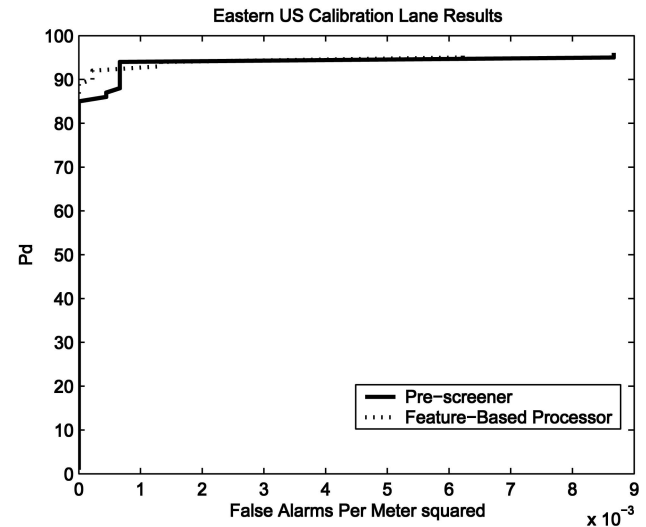|	Eastern Site	Western Site
Square Meters	4500	2000
# of Targets	56	30
Target Types	Plastic & Metal Anti-Tank Mines	Plastic & Metal Anti-Tank Mines

Fig. 13. Pd versus FARs for eastern U.S. site calibration lanes. Pre-screener achieves Pd of 90% at 0.0007 false alarms per meter squared, and feature-based processor achieves 90% Pd at 0.0002 false alarms per meter squared.

in previous blind tests, other vehicular systems using different radars have achieved an FAR of 0.02 false alarms per meter squared at a probability of detection (Pd) of 90%.

Pre-screener and feature based processor results from calibration lanes at the eastern U.S. site can be seen in Fig. 13. These results are aggregate scores over three 500 m × 3 m lanes containing 56 targets buried between 2 in and 6 in in depth. The pre-screener achieves a Pd of 90% at 0.0007 false alarms per meter squared, and the feature-based processor achieves 90% Pd at 0.0002 false alarms per meter squared.

Results for calibration lanes at the western U.S. site for the pre-screener can be seen in Fig. 14. These results represent aggregate scores over two lanes which span 2000 square meters and contain 30 targets buried between 2 in and 6 in in depth. On this data set, the pre-screener achieves Pd of 90% at 0.0005 false alarms per meter squared. Due to the limited number of false alarms available (only 1) on these calibration lanes, the feature-based processor could not be properly trained and could not be run on the data.
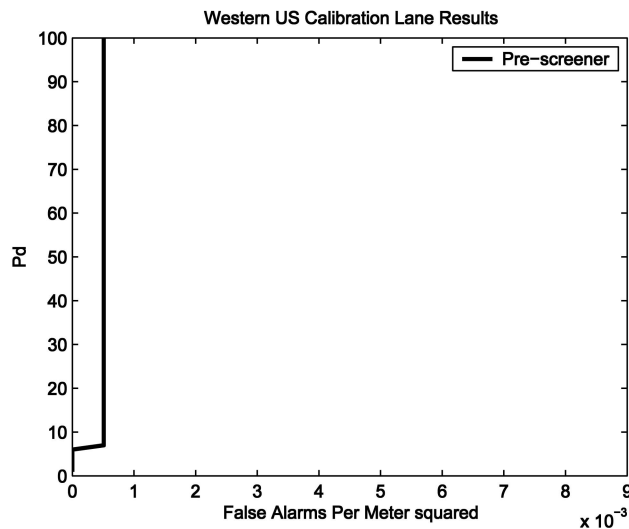
Fig. 14.   Pd versus FARs for western U.S. site calibration lanes. Pre-screener achieves Pd of 90% at 0.0005 false alarms per meter squared, and feature-based processor was not run due to insufficient training data.
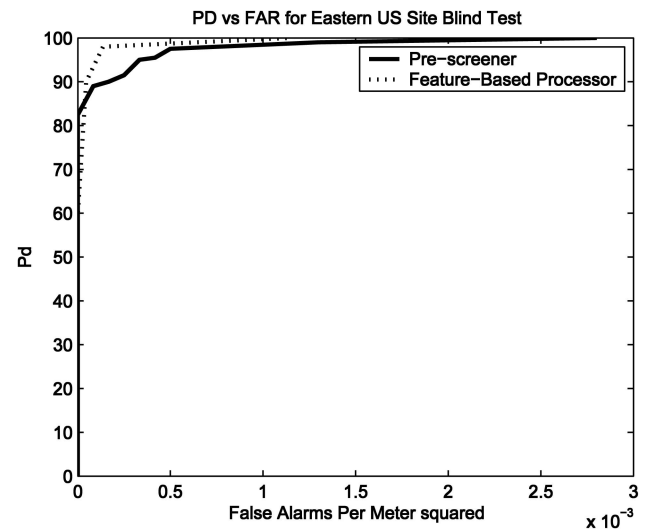

Fig. 15.   Blind test results, eastern site, for LMS pre-screener and feature-based processors. Pre-screener alone achieves Pd of 90% at approximately 0.0002 false alarms per meter squared, while feature-based processor operating on pre-screener generated alarms achieves Pd of 98%, at FAR of approximately 0.0002 false alarms per meter squared.

TABLE IV
Blind Data Collection Specifics

	Eastern Site	Western Site
Square Meters	14000	25000
# of Targets	sequestered	sequestered
Target Types	Plastic & Metal Anti-Tank Mines	Plastic & Metal Anti-Tank Mines

B.   Blind Results

For blind test lanes, data was collected by Niitek and burned to CDs for processing. Resulting alarm files were presented to the independent contractor within 24 h of receiving the data. No modifications were made to the LMS algorithm at any point during or between the two separate test data collections. The ground truth for the blind lanes is sequestered and known only to the government sponsor. Blind test lanes consist of buried (no surface) plastic and metal-cased antitank landmines. Algorithm scores on the blind lanes were generated by the independent contractor. An overview of the blind data collections is shown in Table IV.

In the eastern U.S. site, blind lane performance was comparable to the calibration lane performance, as can be seen in Fig. 15. These scores were generated by the third party contractor and represent aggregate scores over several lanes spanning 14000 square meters. At this site, the pre-screener achieves a Pd of 90% at a false alarm rate of approximately 0.0002 false alarms per meter squared, and the feature-based processor achieves a Pd of 90% at approximately 0.0001 false alarms per meter squared. This performance represents an improvement of
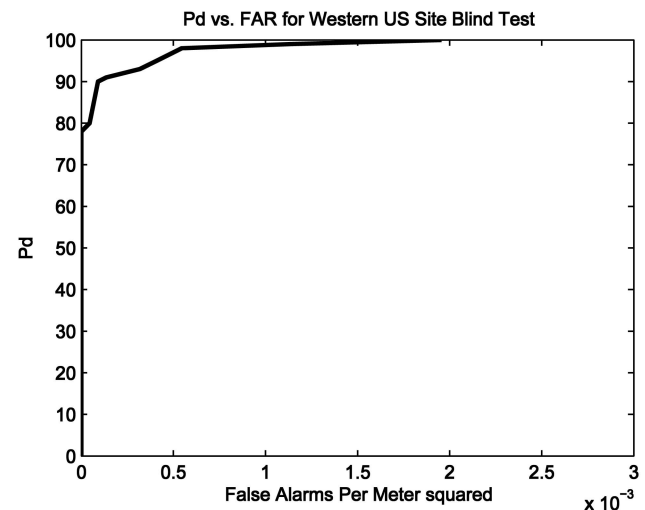

Fig. 16.   Blind test results, western site, for LMS pre-screener. Pre-screener alone achieves Pd of 90% at approximately 0.0001 false alarms per meter squared. Feature results not shown due to lack of training data.

approximately two orders of magnitude over other fielded radar systems.

Results from the western U.S. blind test can be seen in Fig. 16 and represent aggregate scores over several lanes spanning 25000 square meeters. The pre-screener achieves a Pd of 90% at approximately 0.0001 false alarms per meter squared. The feature-based processor was not run on this data due to insufficient training data. Again, this performance represents an improvement of approximately two orders of magnitude over other fielded radar systems.

All results shown so far have been for alarms which have been stitched as discussed in Section IIC.
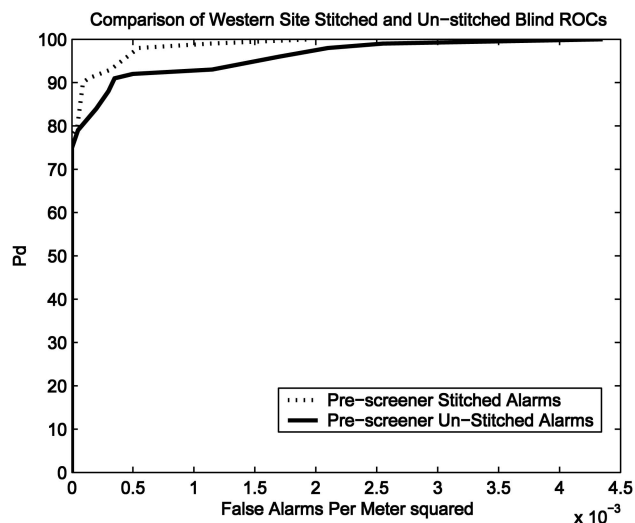
Fig. 17. Difference between ROC curves for stitched and unstitched alarms at western U.S. test site. Although stitching improves performance, the increase is not very significant.
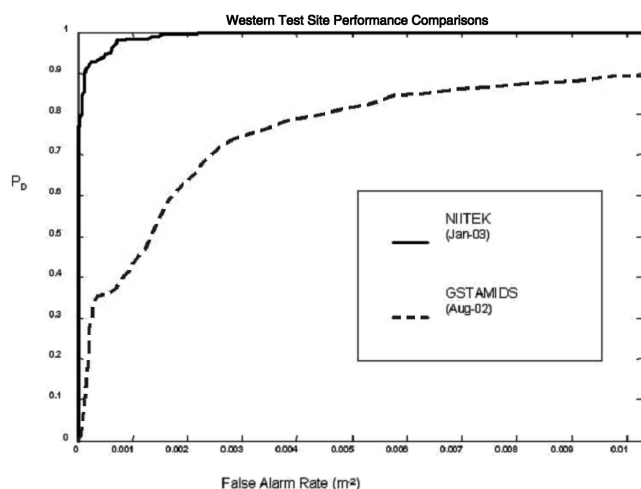

Fig. 18. Performance comparison for NIITEK radar with adaptive LMS processing with previous GSTAMIDS performance on western test site blind data.

The difference between stitched and unstitched scores from the western blind lanes is shown in Fig. 17. Note that although stitching alarms does improve performance, the performance gain does not appear to be very significant.

Finally, we present graphs comparing and contrasting the relative performance of the system under consideration with the algorithm described above with a competing system and algorithm set (the GSTAMIDS radar). Receiver operating characteristics (ROC) curves for these different systems and algorithms processing the same blind data from a western U.S. test site are shown in Fig. 18.

VI. CONCLUSIONS

We have presented a two-stage algorithm for a system for real-time vehicle-mounted GPR landmine detection. The algorithm can be split into a computationally inexpensive pre-screening section and a potentially computationally expensive feature-based discrimination algorithm. The goal of the pre-screening section is to maintain high probability of detection while minimizing the number of potential targets sent to be processed by the feature-based discriminator.

We have shown results from calibration as well as blind lanes which suggest that adaptive pre-screening followed by feature-based processing of Wichmann/Niitek GPR data can achieve FARs far reducing those previously achieved on similar tests. The LMS-based pre-screening algorithm described herein has since been implemented in hardware by Desai and Hintz [46]. It has also been tested against the performance of human observers and been shown to perform at a higher level than most human subjects [47].

Furthermore, although pre-screener results themselves are significant improvements over previous systems, from Fig. 15 it appears that advanced feature-processing techniques can further improve performance at the high probabilities of detection required by the demining problem.

Our future work in this area will consist of alternate feature-based processors for target/natural clutter discrimination, as well as for target/anthropic clutter discrimination.

ACKNOWLEDGMENT

REFERENCES

[1]   UN mine action.
        http://www.mineaction.org/.
[2]   International mine action standards.
        http://www.mineactionstandards.org/.
[3]   Gao, P., Collins, L., Garber, P. M., Geng, N., and Carin, L.
        Classification of landmine-like metal targets using wideband electromagnetic induction.
        IEEE Transactions on Geoscience and Remote Sensing, **38**, 3 (May 2000), 1352–1361.
[4]   Bell, T. H., Barrow, B. J., and Miller, J. T.
        Subsurface discrimination using electromagnetic induction sensors.
        IEEE Transactions on Geoscience and Remote Sensing, **39**, 6 (June 2001), 1286–1293.

[5] Collins, L., Gao, P., and Tantum, S.
Model-based statistical signal processing using electromagnetic induction data for landmine detection and classification.
In *Proceedings of the 11th IEEE Signal Processing Workshop on Statistical Signal Processing*, 2001, 162–165.

[6] Won, I. J., Keiswetter, D. A., and Bell, T. H.
Electromagnetic induction spectroscopy for clearing landmines.
IEEE Transactions on Geoscience and Remote Sensing, **39**, 4 (Apr. 2001), 703–709.

[7] Gao, P., Collins, L., Geng, N., and Carin, L.
Classification of buried metal objects using wideband frequency-domain electromagnetic induction responses: A comparison of optimal and sub-optimal processors.
In *Proceedings of the Geoscience and Remote Sensing Symposium*, vol. 3, 1999, 1819–1822.

[8] Chen, C., Higgins, M. B., O'Neill, K., and Detsch, R.
Ultrawide-bandwidth fully-polarimetric ground penetrating radar classification of subsurface unexploded ordnance.
IEEE Transactions on Geoscience and Remote Sensing, **39**, 6 (June 2001), 1221–1230.

[9] van der Merwe, A., and Gupta, I. J.
A novel signal processing technique for clutter reduction in GPR measurements of small, shallow land mines.
IEEE Transactions on Geoscience and Remote Sensing, **38**, 6 (Nov. 2000), 2627–2637.

[10] Karlsen, B., Larsen, J., Sorensen, H. B. D., and Jakobsen, K. B.
Comparison of PCA and ICA based clutter reduction in GPR systems for anti-personal landmine detection.
In *Proceedings of the 11th IEEE Signal Processing Workshop on Statistical Signal Processing*, 2001, 146–149.

[11] Gader, P. D., Mystkowski, M., and Zhao, Y.
Landmine detection with ground penetrating radar using hidden Markov models.
IEEE Transactions on Geoscience and Remote Sensing, **39**, 6 (June 2001), 1231–1244.

[12] Sabatier, J. M., and Xiang, N.
Investigation of acoustic-to-seismic coupling to detect buried antitank landmines.
IEEE Transactions on Geoscience and Remote Sensing, **39**, 6 (June 2001), 1146–1154.

[13] Datema, C. P., Bom, V. R., and van Eijk, C. W. E.
Landmine detection with the neutron backscattering method.
IEEE Transactions on Nuclear Science, **48**, 4 (Aug. 2001), 1087–1091.

[14] van Kempen, L., and Sahli, H.
Signal processing techniques for clutter parameters estimation and clutter removal in GPR data for landmine detection.
In *Proceedings of the 11th IEEE Signal Processing Workshop on Statistical Signal Processing*, 2001, 158–161.

[15] Homer, J., Tang, H. T., and Longstaff, I. D.
Radar imaging of shallow buried objects.
In *Proceedings of Geoscience and Remote Sensing Symposium IGARSS '99 Proceedings*, vol. 5, 1999, 2477–2479.

[16] Halman, J. I., Shubert, K. A., and Ruck, G. T.
SAR processing of ground-penetrating radar data for buried uxo detection: Results from a surface-based system.
IEEE Transactions on Antennas and Propagation, **46**, 7 (July 1998), 1023–1027.

[17] Wang, Y., Longstaff, I. D., and Leat, C. J.
SAR imaging of buried objects from mom modelled scattered field.
In *IEE Proceedings on Radar, Sonar and Navigation*, vol. 148, June 2001, 167–172.

[18] Stickley, G. F., Longstaff, I. D., and Radcliffe, M. J.
Synthetic aperture radar for the detection of shallow buried objects.
In *The Detection of Abandoned Land Mines: A Humanitarian Imperative Seeking a Technical Solution, EUREL International Conference*, 431, Oct. 1996, 160–163.

[19] Budko, N. V., Remis, R. F., and van Den Berg, P. M.
Advances in GPR data processing for antipersonnel landmine detection.
In *Proceedings of the Geoscience and Remote Sensing Symposium*, vol. 1, 2000, 24–28.

[20] Xu, X., and Miller, E. L.
Adaptive difference of gaussians to improve subsurface object detection using GPR imagery.
In *Proceedings of the International Conference on Image Processing*, vol. 2, Sept. 2002, 457–460.

[21] Xu, X., Miller, E. L., Rappaport, C. M., and Sower, G. D.
Statistical method to detect subsurface objects using array ground-penetrating radar data.
IEEE Transactions on Geoscience and Remote Sensing, **40**, 4 (Apr. 2002), 963–976.

[22] Kovalenko, V., and Masalov, S. A.
2D matrix filtering of ground penetrating radar data.
In *Proceedings of International Conference on Mathematical Methods in Electromagnetic Theory*, vol. 1, Sept. 2000, 236–238.

[23] Xu, X., and Miller, E. L.
On the use of contrast stretch and adaptive filter to enhance ground penetrating radar imagery.
In *Proceedings of IEEE International Geoscience and Remote Sensing Symposium*, vol. 6, June 2002, 3585–3587.

[24] Zoubir, A. M., Chant, I. J., Brown, C. L., Barkat, B., and Abeynayake, C.
Signal processing techniques for landmine detection using impulse ground penetrating radar.
IEEE Sensors Journal, **2**, 1 (Feb. 2002), 41–51.

[25] O'Neill, K.
Discrimination of uxo in soil using broadband polarimetric GPR backscatter.
IEEE Transactions on Geoscience and Remote Sensing, **39**, 2 (Feb. 2001), 356–367.

[26] Carevic, D.
Wavelet-based method for detection of shallowly buried objects from GPR data.
In *Proceedings on Information, Decision and Control*, Feb. 1999, 201–206.

[27] Perrin, S., Bibaut, A., Duflos, E., and Vanheeghe, P.
Use of wavelets for ground-penetrating radar signal analysis and multisensor fusion in the frame of land mine detection.
In *Proceedings of IEEE International Conference on Systems, Man, and Cybernetics*, vol. 4, Oct. 2000, 2940–2945.

[28] Chen, C-C., Peters, L., Jr., and Burnside, W. D.
Ground penetration radar target classification via complex natural resonances.
In *Proceedings of Antennas and Propagation Society International Symposium*, vol. 3, June 1995, 1586–1589.

[29] Carevic, D., Chant, I., and Caelli, T.
Feature extraction and classification of minelike targets
from GPR data using Gaussian mixture models.
In *Proceedings on Information, Decision and Control*, Feb.
1999, 329–334.

[30] Gader, P. D., Keller, J. M., and Nelson, B. N.
Recognition technology for the detection of buried land
mines.
IEEE Transactions on Fuzzy Systems, **9**, 1 (Feb. 2001),
31–43.

[31] Frigui, H., Gader, P., and Keller, J.
Fuzzy clustering for land mine detection.
In *Proceedings of the Conference of the North American
Fuzzy Information Processing Society—NAFIPS*, Aug.
1998, 261–265.

[32] Gader, P., Grandhi, R., Lee, W-H., and Wilson, J. N.
Feature analysis of NIITEK ground penetrating radar
using order weighted averaging operations for landmine
detection.
In *Proceedings of the SPIE Detection and Remediation
Technologies for Mines and Minelike Targets IX*, vol. 5415,
2004, 953–962.

[33] Hintz, K. J.
SNR improvements in NIITEK ground penetrating radar.
In *Proceedings of the SPIE Detection and Remediation
Technologies for Mines and Minelike Targets IX*, vol. 5415,
2004, 399–408.

[34] Legarsky, J. J., Broach, J. T., and Bishop, S. S.
Processing of GPR data from NIITEK landmine detection
system.
In *Proceedings of the SPIE Detection and Remediation
Technologies for Mines and Minelike Targets VIII*, vol.
5089, 2003, 1375–1382.

[35] Lang, D. A., Dustin, B. M., Torrione, P. A., and Collins,
L. M.
Three-dimensional features to improve detection using
ground-penetrating radar.
In *Proceedings of the SPIE Detection and Remediation
Technologies for Mines and Minelike Targets IX*, vol. 5415,
2004, 953–962.

[36] Niitek, Inc.
Niitek web page. http://www.niitek.com.

[37] Howard, P., and Clodfelter, F.
Countermine test management system.
BRTRC, Technology Research Corporation, 8260 Willow
Oaks Corporate Drive, Suite 800, Fairfax, VA, 22031,
2002.

[38] French, P. A., Zeidler, J. R., and Ku, W. H.
Enhanced detectability of small objects in correlated
clutter using an improved 2-D adaptive lattice algorithm.
IEEE Transactions in Image Processing, **6**, 3 (Mar. 1997),
383–397.

[39] Ohki, M., and Hashiguchi, S.
Two-dimensional LMS adaptive filters.
IEEE Transactions on Consumer Electronics, **37**, 1 (Feb.
1991), 66–73.

[40] Chen, S-G., and Kao, Y-A.
A new efficient 2-d LMS adaptive filtering algorithm.
In *Proceedings of IEEE International Symposium on
Circuits and Systems*, vol. 1, May 1993, 299–302.

[41] Abrahamsson, R., Larsson, E. G., Li, J., Habersar, J.,
Maksymonko, G., and Bradley, M.
Elimination of leakage and ground bounce effects in
ground-penetrating radar.
In *Proceedings of the 11th IEEE Signal Processing
Workshop on Statistical Signal Processing*, 2001, 150–153.

[42] Wu, R., Clement, A., Li, J., Larsson, E. G., Bradley, M.,
Habersat, K., and Maksymonko, G.
Adaptive ground bounce removal.
Electronics Letters, **37**, 20 (Sept. 2001), 1250–1252.

[43] Haykin, S.
Adaptive Filter Theory (3rd ed.).
Upper Saddle River, NJ: Prentice-Hall, 1996.

[44] Gader, P., Wilson, J., and Lee, W-H.
Adaptive whitening for landmine detection with
array-based ground penetrating radar.
In *Proceedings of Detection and Remediation Technologies
for Mines and Minelike Targets VII Conference, 2003
International Symposium on Aerospace/Defense Sensing
and Controls*, Apr. 2003.

[45] Gader, P., Lee, W-H., and Wislon, J. N.
Detecting landmines with ground-penetrating radar
using feature-based rules, order statistics, and adaptive
whitening.
IEEE Transactions on Geoscience and Remote Sensing, **42**,
11 (Nov. 2004), 2522–2534.

[46] Desai, T. J., and Hintz, K. J.
A parallel implementation of LMS adaptive filter in
hardware for landmine detection.
In *Proceedings of the SPIE Detection and Remediation
Technologies for Mines and Minelike Targets IX*, vol. 5415,
Sept. 2004, 973–983.

[47] Throckmorton, C. S., Torrione, P. A., Collins, L. M., Gader,
P. D., Lee, W-H., and Wilson, J. N.
The efficacy of human observation for discrimination and
feature identification of targets measured by the NIITEK
ground penetrating radar.
In *Proceedings of the SPIE Detection and Remediation
Technologies for Mines and Minelike Targets IX*, vol. 5415,
Sept. 2004, 963–972.

Peter Torrione received the B.S.E.E. degree from Tufts University, Medford, MA, in 1999, and the M.S.E.E. degree from Duke University, Durham, NC, in 2002.

From 2002 to 2004 he was an associate in research at Duke University. He currently attends Duke University where he is pursuing his Ph.D. degree in electrical and computer engineering.

Chandra Throckmorton completed the B.S.E.E. at the University of Texas at Arlington in December 1995, and received the M.S.E.E. in May 1998, and the Ph.D. in December 2001 both from Duke University, Durham, NC.

From 2002 to 2004, she was a research associate at Duke University. She is currently a research scientist at Duke University with research interests in statistical signal processing for detection and classification as well as designing methods to improve speech comprehension for cochlear implant recipients.

Leslie Collins (M'96—SM'01) was born in Raleigh, NC. She received the B.S.E.E. degree from the University of Kentucky, Lexington, and the M.S.E.E. and Ph.D. degrees in electrical engineering, both from the University of Michigan, Ann Arbor.

She was a senior engineer with the Westinghouse Research and Development Center, Pittsburgh, PA, from 1986 to 1990. In 1995 she became an assistant professor in the Electrical and Computer Engineering Department, Duke University, Durham, NC, and has been an associate professor in ECE since 2002. Her current research interests include incorporating physics-based models into statistical signal processing algorithms, and she is pursuing applications in subsurface sensing as well as enhancing speech understanding by hearing impaired individuals.

Dr. Collins is a member of the Tau Beta Pi, Eta Kappa Nu, and Sigma Xi honor societies.